

Quantum Time Transfer For Freespace Quantum Networking

Randy Lafler¹ and R. Nicholas Lanning¹

¹*Air Force Research Laboratory, Directed Energy Directorate, Kirtland AFB, NM, United States**
(Dated: November 3, 2022)

Timing requirements for long-range quantum networking are driven by the necessity of synchronizing the arrival of photons, from independent sources, for Bell-state measurements. Thus, characteristics such as repetition rate and pulse duration influence the precision required to enable quantum networking tasks such as teleportation and entanglement swapping. Some solutions have been proposed utilizing classical laser pulses, frequency combs, and bi-photon sources. In this article, we explore the utility of the latter method since it is based upon quantum phenomena, which makes it naturally covert, and potentially quantum secure. Furthermore, it relies on relatively low technology quantum-photon sources and detection equipment, but provides picosecond timing precision even under high loss and high noise channel conditions representative of daytime space-Earth links. Therefore, this method is potentially relevant for daytime space-Earth quantum networking and/or providing high-precision secure timing in GPS denied environments.

I. INTRODUCTION

Precise synchronization of remote clocks is at the heart of position, navigation, and timing (PNT), high speed transactions, distributed computing, and as of late, quantum networking. To enable *global-scale* quantum networking, one needs to distribute entanglement between distant quantum nodes [1, 2], which will likely require a series of entanglement swapping operations between different arrangements of Earth and satellite quantum nodes [3, 4]. If ultra-narrow spectral filtering is utilized, then each entanglement swapping operation could require Bell-state measurements with as little as nanosecond-scale timing precision. This can be achieved utilizing single-photon avalanche diode (SPAD) detectors and synchronization provided by current global positioning system (GPS) public signals [5]. However, ultra-narrow spectral filtering is not currently compatible with entangled photon sources, which are broader band, and would result in considerable attenuation. An alternate approach is to increase the timing precision to the picosecond or femtosecond level, along with choosing the appropriate pulse duration and spectral-temporal filtering. This would result in a higher probability of success per pulse and maintain the rejection of noise photons that scatter into the channel. Therefore, techniques to precisely synchronize remote clocks are an important ongoing area of research.

Perhaps the most straight forward optical-time-transfer technique uses pulsed lasers, single photon detectors, and software-based correlation methods. For example, time transfer by laser link (T2LE) demonstrations have achieved picosecond-scale precision between remote ground stations operating in common view with the Jason-2 satellite [6]. In contrast, there are also hardware-

based methods such as optical two-way time and frequency transfer (O-TWTFT) [7, 8], which utilizes frequency combs and linear optical sampling to synchronize two remote clocks to femtosecond precision. However, to date, demonstrations of O-TWTFT have been performed between stationary sites [7, 8] or slow moving drones, < 25 m/s. The conclusions in Refs. [9, 10] suggest that O-TWTFT can maintain femtosecond-scale precision despite the high orbital velocities and non-reciprocity of two-way Earth-satellite links, but a demonstration over channel conditions representative of an earth-satellite link has yet to be performed.

The concept of using quantum phenomena has also emerged as a possible solution for precise synchronization. One example is the Earth-satellite synchronization demonstration that used quantum key distribution (QKD) with attenuated laser pulses and a high powered sync pulse [11]. However, this technique relies on extraneous components and classical phenomenon making it more complex, less covert, and not genuinely quantum. Another example relies on Hong-Oh-Mandel (HOM) quantum interference between entangled photon pairs [12]. However, it is challenging to utilize this technique over freespace-atmospheric channels due to aberrations of the photon transverse momentum and the very high level of attenuation characteristic of the double-pass geometry.

Another technique consists of utilizing the femtosecond-scale temporal correlations of photon pairs created in spontaneous-parametric-down conversion (SPDC) photon sources. In this case, the relative time offset between two remote clocks is measured with the following procedure: (1) a series of photon pairs are separated and transmitted to two remote sites, (2) the photons are detected and their arrival times time tagged based on the respective local clock, (3) after enough detection events are collected, the series of arrival times from each site are combined and correlation methods are used to find the clock offset. This technique was first proposed in Refs. [13, 14] and it is referred to as quantum time transfer (QTT) for the remainder of this

* AFRL.RDSS.OrgMailbox@us.af.mil
DISTRIBUTION A: Approved for public release; distribution is unlimited. Public Affairs release approval AFRL-2022-5234

paper. In the continuous wave (CW) biphoton-source mode of operation, one-way QTT [13] can provide relative clock synchronization, and two-way QTT [14] can provide absolute clock synchronization. One could think of QTT as a quantum analog of T2L2, where the laser pulses of T2L2 are replaced with randomly arriving, but correlated, photon pairs.

QTT can also be distinguished from other optical-time transfer techniques because there are methods to make it quantum secure. If the QTT-photon source is also entangled, then one could monitor an entanglement measure to detect an eavesdropper, and thus attempts to spoof the QTT. For example, if the photon source is polarization entangled, then the time tagging detector arrangements could be modified to discriminate polarization and monitor a Bell inequality. Similarly, one could utilize techniques from energy-time entanglement-based high-dimensional quantum key distribution (HDQKD) [15–17] and achieve quantum security by monitoring the energy-time entanglement. Altogether, QTT has potential that warrants further investigation as to its utility for extreme quantum networking conditions with limited additional equipment.

In this article, we investigate a simple and computationally fast method of QTT as follows. In Sec. II we introduce a potential use-case architecture, outline the algorithm, and discuss the expected precision. In Sec. III we assume several different heralding efficiency sources and perform a simulation spanning a large space of channel attenuation and noise photons. We consequently discuss the probability of success per acquisition, the standard error of the mean (SEM) of the measured clock offset, and the overlapping Allan deviation, which conveys the stability and noise profile of the two clock system. In Sec. IV we interpret the results in the context of sky-noise photons and slant-path turbulence corresponding to a space-to-Earth downlink, thereby demonstrating the relevance of our method for global-scale quantum networking.

II. QUANTUM TIME TRANSFER

A. Example Architecture

QTT has several advantages over the aforementioned techniques that make it promising for *freespace* channels. Namely, the architecture is relatively simple, low size, weight, and power (SWAP), and the algorithm is robust to loss and noise photons. Figure 1 depicts some of the relevant components and phenomena comprising QTT over daytime-freespace channels. Alice and Bob both utilize SPAD detectors, time-tagging units, and Rubidium frequency standards (RbFS) to provide initial system stability, which is discussed more in the following subsection. Alice records one of the biphotons locally subsequent to

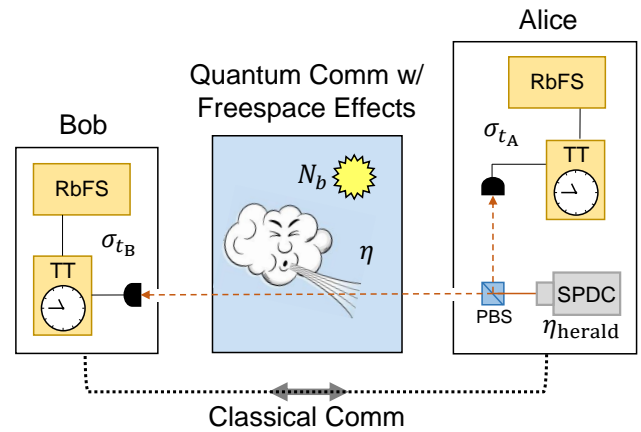


FIG. 1: Block diagram depicting some relevant components and phenomenon when performing QTT over daytime atmospheric channels. Alice uses a Type-II SPDC biphoton source to create temporal correlations that facilitate QTT. She keeps one of the biphotons locally and records its detection time with a detection system consisting of a detector, a time tagger (TT), and Rubidium frequency standard (RbFS), collectively with jitter σ_{t_A} . With heralding efficiency η_{herald} she sends the companion photon to Bob who similarly records the detection event, subsequent to his channel attenuation η_B , caused in part by atmospheric effects, and the presence of sky noise photons N_b that scatter into the channel. Bob announces the time tags over a classical channel and Alice uses this information to perform a correlation measurement to determine Bob’s relative offset, Δt .

spectral, detector, and heralding efficiencies

$$\eta_A = \eta_{\text{spec}} \eta_{\text{det}} \eta_{\text{herald}}, \quad (1)$$

and Bob similarly records detection events with extra attenuation imposed by the optical receiver and freespace channel

$$\eta_B = \eta_{\text{spec}} \eta_{\text{det}} \eta_{\text{herald}} \eta_{\text{rec}} \eta_{\text{channel}}. \quad (2)$$

Background-noise photons N_b , which can be calculated using radiometric equations [18], scatter to Bob’s detector subsequent to attenuation $\eta_{\text{spec}} \eta_{\text{det}} \eta_{\text{rec}}$. Figure 2(a) shows the effect of these phenomenon on the time series of detection events registered by Bob. Alice records a stream of detection events represented by the antenna in the top row. Bob records the same events as Alice with efficiency η_B . In Bob’s stream, potential detection events that are lost are grayed out, and events corresponding to background noise photons are colored red. The infrequent true coincidences that give rise to a correlation signal at Δt are colored green.

B. Algorithm

The QTT algorithm presented in Ref. [13] measures the total clock offset Δt with a series of increasingly precise cross-correlations. The algorithm can be summarized as follows. First, judiciously choose an acquisition time depending on the rate of Alice and Bob’s detection events and divide it into an empty array of N bins of width w , one array each for Alice and Bob. Second, for each array assign a 1 to every bin where a time-tag is present and a 0 otherwise. Third, calculate the discrete cross-correlation of the arrays to find a peak that corresponds to the relative offset between the Alice and Bob clocks. The algorithm can be repeated again with a narrower bin width to increase the measurement precision, but it is very sensitive to the choice of bin size, acquisition time, etc. In the regime of high channel attenuation, high background rates, and large, unknown Δt , we found this algorithm to be difficult to optimize and extremely computationally intensive. This is because a very large number of bins, $N > 2^{24}$, are required to isolate enough “true” coincidences from the randomly arriving background photons in order to boost the correlation peak above the noise.

In order to investigate the extreme conditions of daytime-freespace quantum links, we developed the following coincidence finding algorithm that is based on a simple arrival-time-difference histogram. This algorithm is quick, computationally efficient, and maintains sub-nanosecond timing precision over the relevant parameter space:

1. Concatenate Alice and Bob time-tag arrays, t_A and t_B , respectively, and sort the resulting array M from earliest to latest time.
2. Find the indexes $\{k\}$ of t_B in M .
3. Calculate the time differences between all of the Bob times $M_{\{k\}}$ and adjacent times up to n indexes preceding and trailing each Bob time, i.e.,

$$\tau_{ik}^{(\pm)} = M_{k \pm i} - M_k, \quad (3)$$

for all k and for $i = 0$ to n .

4. Histogram the resulting time differences τ_{ik} with bin size τ_{hist} and over the range $-\tau_a$ to τ_a .
5. When the algorithm is successful, there is a Gaussian feature in the histogram in which the mean corresponds to the relative clock offset $\Delta t \equiv \bar{\tau}$ with standard deviation $\sigma_{\Delta t} \equiv \sigma_{\tau}$ corresponding to the system jitter. The SEM of Δt is discussed later in Sec. II C.

QTT can be used as a stand-alone protocol, or underpin other quantum protocols, such as entanglement based QKD or entanglement distribution. In the latter case, one would want to find and isolate the coincidence detection events from the background, and use them for

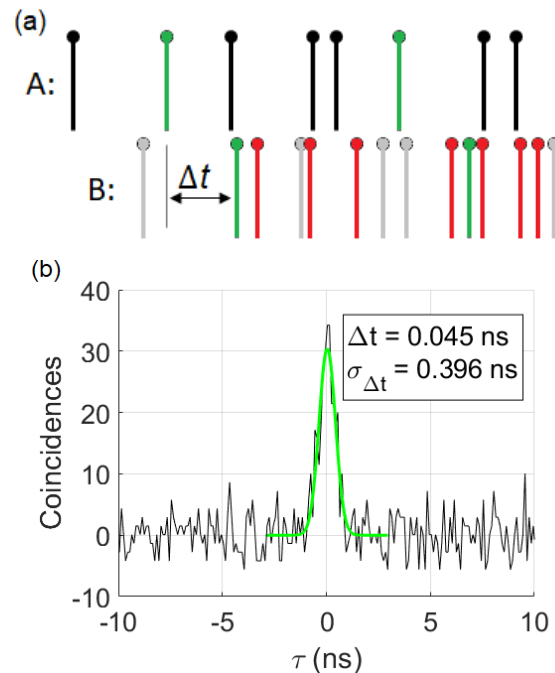


FIG. 2: (a) Data stream depicting the phenomenon underpinning QTT. Alice records a stream of detection events represented by the antenna (see top row). Bob records the same events as Alice with efficiency η_B (see bottom row). In Bob’s stream, potential detection events that are lost are grayed out, and events corresponding to background noise photons are colored red. The infrequent true coincidences that give rise to a correlation peak at Δt are colored green. (b) A histogram of detection time differences τ , which reveals an example of a correlation peak (black curve). The green curve is a Gaussian fit to the correlation peak, which establishes the clock offset $\Delta t \equiv \bar{\tau}$ and its standard deviation $\sigma_{\Delta t} \equiv \sigma_{\tau}$ resulting from the total systematic detection time jitter (see Sec. II C).

further processing. To do this, Bob can align his time tags t_B to Alice’s clock according to,

$$t'_B = (t_B + \Delta t) \cdot (1 + \Delta U), \quad (4)$$

where t'_B are Bob’s synchronized time tags. ΔU is the clock drift, i.e. the fractional frequency deviation, which can be estimated by subtracting successive clock offset measurements Δt_i and dividing by the acquisition time,

$$\Delta U = \frac{\Delta t_{i+1} - \Delta t_i}{T_{\text{acq}}}. \quad (5)$$

If instead one performs QTT in both directions, i.e. two-way QTT, the propagation time can be measure and the clocks can be synchronized absolutely [14].

One must take care that the clock drift ΔU is relatively small and constant during an acquisition time T_{acq} , such that true coincidences do not drift outside of the coincidence peak and reduce the coincidence signal. Therefore,

the acquisition time T_{acq} should be chosen small enough so that the product of the clock drift ΔU and the acquisition window T_{acq} is less than the width of the coincidence peak. However, a longer acquisition time T_{acq} is also advantageous because the time series will contain more true coincidences. If the clock drift ΔU follows a predictable trend, then one method to allow for a larger acquisition time T_{acq} is to preemptively remove ΔU from Bob's time series via Eq. 4 before performing QTT. In the next section, we will show that for the case of photon detection with SPAD detectors and 1 second acquisition time T_{acq} , the width of the coincidence peak is about 1 ns, which constrains the clock drift ΔU to be smaller than 10^{-9} . Therefore, in practice one will need highly stable frequency references, such as a RbFSs, in order to sufficiently reduce the clock drift ΔU .

C. Precision

Our QTT algorithm results in a Gaussian correlation feature with mean equal to the clock offset Δt and standard deviation $\sigma_{\Delta t}$ corresponding to the total systematic error of the system (see Fig. 2(b)). Consequently, one would expect the timing precision to follow the SEM given by

$$SEM = \sigma_{\Delta t} / \sqrt{N_T}, \quad (6)$$

where $N_T = N_C - N_{\text{AC}}$ is an estimate of the number of true coincidences, N_C is the number of measured coincidences, and N_{AC} is an estimate of the number of accidental coincidences.

The systematic timing error of all the detection components modeled in our system is

$$\sigma_t^{(\text{sys})} = \sqrt{\sigma_{t_A}^2 + \sigma_{t_B}^2}, \quad (7)$$

where σ_{t_A} and σ_{t_B} are the timing jitters of Alice and Bob's systems, respectively. In our simulation we assume $\sigma_{t_A} = \sigma_{t_B}$ and total system jitter $\sigma_t^{(\text{sys})} = 405$ ps, see the following section for details. In Fig. 2(b) we present an example correlation for a 2-MHz source with channel attenuation $\eta_B = -23$ dB and $N_b \approx 9 \times 10^5$. From the Gaussian fit we see that $\sigma_{\Delta t} = 396$ ps, which is consistent with the systematic jitter $\sigma_t^{(\text{sys})}$ within the fitting errors. In fact, the correlation width is characteristic of the system and is relatively unchanged regardless of the channel conditions. Therefore, the width of the correlation feature can be used as a test to determine if the algorithm was successful. For example, if QTT and the peak finding algorithm obtain a noise peak, then the width would likely be much narrower than a true peak, and the erroneous Δt could be disregarded. We use this technique to find the probability of success in Sec. III A.

III. SIMULATION

We investigate the performance of QTT for sources with varying heralding efficiencies. This is a pivotal consideration, because unlike sky noise photons that can be filtered with tighter spectral and spatial filtering, the photon source itself produces noise photons perfectly in band with probability $1 - \eta_{\text{herald}}$. We consider four different 2 MHz pair rate sources with heralding efficiencies that range from readily available commercial-off-the-shelf units to specialized one-off devices, namely 20%, 40%, 60%, and 80%, respectively. Without loss of generality we set the clock offset Δt to zero. For simplicity, and to reduce the parameter space, we also set the clock drift ΔU to zero. Consequently, the results we present can be considered a best-case-scenario, and we reserve the study of performance degradation with non-zero clock drift ΔU for future work.

We span a 2D parameter space of channel attenuation and background noise photons repeating each channel condition 100 times to find statistically relevant quantities. For each channel condition we examine the probability of success, which is the number of times the QTT algorithm correctly identified the clock offset. We then find the threshold attenuation η_{th} that maintains $\geq 99\%$ probability of success. The threshold η_{th} is further investigated in relationship to the heralding efficiency, channel attenuation, background noise, and true coincidences. We then fix the background rate N_b and we investigate the relationship between the SEM and the number of true coincidences N_T . Lastly, we fix the channel conditions and discuss the timing stability by calculating the overlapping Allan deviation.

Each of the Alice and Bob time series are generated in the following way. First, given the source rate $R = 2$ MHz and acquisition time $T_{\text{acq}} = 1$ sec, we create an array of 2 million uniformly distributed random times between 0 and 1. The array is then sorted from smallest to largest time, becoming the unattenuated Alice time series. An identical copy is made for Bob, which would be shifted appropriately relative to the Alice time series for cases where the clock offset Δt is non-zero. The effects of the total systematic timing jitter are now included by adding a Gaussian distributed random variable with standard deviation σ_{t_A} or σ_{t_B} to each time tag of the Alice and Bob's time series, respectively. Unless otherwise noted, we assume SPAD detectors and time taggers with timing jitter $\sigma_t^{(\text{det})} = 287$ ps and $\sigma_t^{(\text{tt})} = 4$ ps, respectively. Next, time tags are randomly removed from Alice and Bob's time series equivalent to their respective channel attenuation. Alice's attenuation is set to the product of the detection efficiency $\eta_{\text{det}} = 0.6$ and the losses due to the transmission of the spectral filter $\eta_{\text{spec}} = 0.9$. Bob's channel attenuation and background noise photons are set to values commensurate with a daytime space-to-Earth downlink. Lastly, we include the effect of the total system deadtime, where we remove all time tags that are within 84 ns of another time tag from the Alice

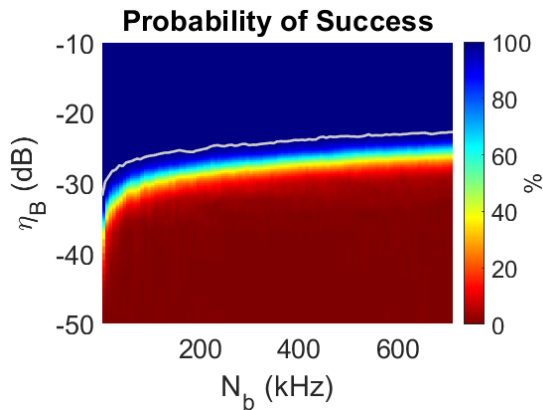


FIG. 3: Density plot giving the probability of successful QTT as a function of Bob’s total channel attenuation η_B and background counts N_b , for a source with $\eta_{\text{herald}} = 20\%$. The gray line traces out the 99% probability of success.

and Bob time series. We chose a deadtime of 84 ns to match the total systematic deadtime that we have measured with our experimental system. The deadtime is a very important effect to include, because as the heralding efficiency or the background rate at Bob increases, the probability of detecting both photons of a pair decreases. Consequently, the performance of QTT is very sensitive to the deadtime, and a thorough investigation should be included in any system model or design.

A. Probability of Success

The probability of success, for each channel condition, is the fraction of the total trials in which the correct offset Δt and correlation width $\sigma_{\Delta t}$ were measured. A more rigorous way to determine the probability of success is through a bootstrapping technique. For example, one could compare the signal peak height, number of coincidences, or another metric with a noise distribution, which is derived by bootstrapping the QTT algorithm on uncorrelated versions of the data. A simple method to generate effectively uncorrelated data sets from the measured data is to apply a large, random offset $\Delta t \gg t_a$ to the Bob time series, which will cause the QTT algorithm to find only accidental coincidences. Once the bootstrapping distribution is calculated, one can calculate the probability that uncorrelated data could have given rise to the metric, and therefore the probability the QTT algorithm was successful. The issue is that bootstrapping is time consuming, computationally expensive, and therefore might be difficult to implement in a real-time experiment. Nevertheless, for our simulation the aforementioned method suffices.

In Fig. 3(a) we assume a 20% heralding efficiency source and show the probability of success as a function of attenuation and the number of noise photons. The

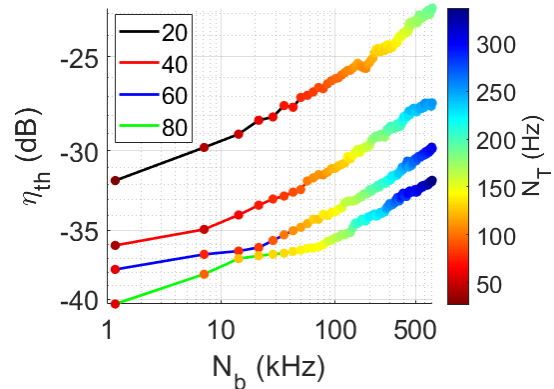


FIG. 4: Curves giving the threshold attenuation η_{th} that maintains $\geq 99\%$ probability of success as the number of sky background photons increases. The black, red, blue, and green curves correspond to 20, 40, 60, and 80% heralding efficiency, respectively. The marker colors correspond to the number of true coincidences for each of the channel conditions.

gray line traces out the 99% probability of success. This shows that the QTT algorithm is highly robust to sky noise background and is much more susceptible to channel loss as seen by the abrupt drop in performance with increasing channel attenuation η_B .

B. Threshold Attenuation

In Fig. 4 we plot the greatest channel attenuation η_{th} possible while maintaining 99% probability of success for 20%, 40%, 60%, and 80% heralding efficiency. For each heralding efficiency, the marker color indicates the number of true coincidences N_T . We see that as the heralding efficiency increases so does the magnitude of the threshold attenuation η_{th} . This is because higher heralding efficiencies correspond to larger true coincidence rates N_T and therefore larger coincidence peaks. We see the QTT algorithm achieves 99% success probability despite 100-kHz scale background-noise photons N_b compared to only a few hundred received true coincidences N_T . This is because the sky background noise photons are uncorrelated with the true coincidences and their contribution to the histogram is spread out uniformly over the entire τ_a range. Considered another way, QTT can be thought of as a narrow temporal filter, rejecting sky background with high efficiency.

C. SEM

To investigate the QTT SEM, we fix the number of background photons N_b to ~ 2 MHz and perform a Monte Carlo simulation. We calculate the standard deviation of

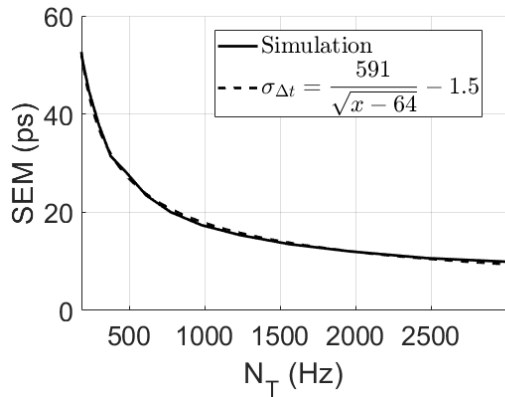


FIG. 5: The SEM clock offset as a function of the number of “true” coincidences N_T (i.e., with accidentals subtracted), where the number of background photons are set to $N_b = 2.14$ MHz. On the black curve, each SEM is calculated by taking the standard deviation of the clock offsets measured from a Monte Carlo simulation with 1000 trials. The dashed curve is the fit and the fit parameters are given in the plot legend.

1000 independent clock offset measurements as a function of true coincidences N_T . The resulting estimate of the SEM is given by the black curve in Fig. 5. The fit is given by the dashed curve and the fit parameters are given in the legend. The fit reveals the characteristic $1/\sqrt{N_T}$ dependence of Eq. 6, but the numerator of the fit, 591 ps, is about a factor of $\sqrt{2}$ times larger than $\sigma_{\Delta t}$. This discrepancy could be the result of a limited number of Monte Carlo trials, an unknown bias in the estimate of the number of true coincidences, the non-gaussian nature of the deadtime losses, or another phenomenon that has yet to be identified. Nevertheless, Fig. 5 shows that the timing precision of a single-shot clock offset measurement Δt can be estimated with the SEM (see Eq. 6), but may need to be modeled directly depending on the source and channel conditions.

D. Allan Deviation

The Allan deviation is a standard method to characterize the stability of a clock system. When the Allan deviation is plotted on a log-log scale, the slope of the curve indicates the type of noise in the system. Figure 6 shows the overlapping Allan deviation [19] with channel attenuation $\eta_B = -23$ dB and background rate N_b at 2.14 MHz. The black curve corresponds to SPAD detectors with 287-ps jitter, the green curve to nanowire detectors with 22-ps jitter, and the legend shows the linear fit of each. The negative 0.5 slope indicates Gaussian noise, which is the noise profile we use to model the detection jitter [20]. It also shows that the system can achieve ps-level stability with SPAD detectors in 40 seconds, and

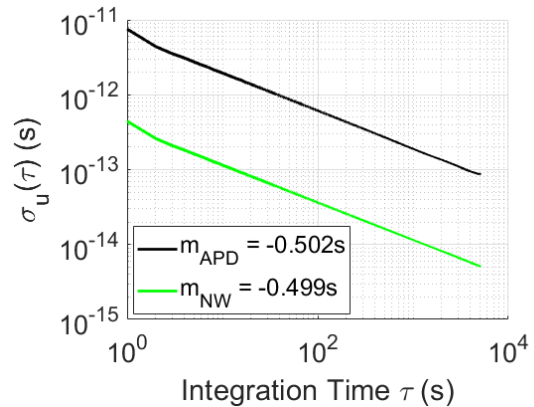


FIG. 6: The overlapping Allan deviation $\sigma_u(\tau)$ for channel attenuation $\eta_{\text{atmos}} = -23$ dB and sky background rate $N_b = 2.14$ MHz with photon detection jitter characteristic of SPADs (black curve) and superconducting nanowire detectors (green curve). As expected, the slope of the line $-1/2$ is representative of Gaussian noise [20]. This simulation assumes perfect clock drift correction, i.e. $\Delta U = 0$.

fs-level stability with nanowire detectors in 5000 seconds. The effects of residual clock drift jitter are reserved for future work.

IV. RELEVANCE TO SPACE-EARTH CHANNELS

To demonstrate the applicability of our QTT algorithm and simulation, we apply our results to a daytime space-to-Earth quantum downlink architecture. We assume a satellite in a 600-km circular orbit has a 15-cm transmit aperture and propagates 780-nm photons to a ground station with a 1-m receive aperture utilizing a 1-nm spectral filter. It is assumed that all the detectors in the system have efficiency $\eta_{\text{det}} = 0.6$, the spectral filters have efficiency $\eta_{\text{spec}} = 0.9$, and the ground station receiver has efficiency $\eta_{\text{rec}} = 0.5$. The angle dependent atmospheric transmission efficiency η_{trans} and the background sky radiance H_b are generated in MODTRAN for a high desert climate with urban aerosols. We assume that conventional methods for establishing frequency stability in GPS satellites can be employed in a QTT downlink [21]. This would allow ΔU to meet the threshold discussed in Sec. II B, and establish the relevance of our $\Delta U = 0$ simulation for this down-link architecture, at least as a first order study.

In Ref. [22] we establish a theoretical framework in which the receiver performance is modeled as a function of atmospheric phenomenon and adaptive optics (AO) system parameters. It uses scaling law equations to estimate the residual error, after wavefront correction, and determine how the error inhibits the ability to transmit the signal light through a small spatial filter in the focal

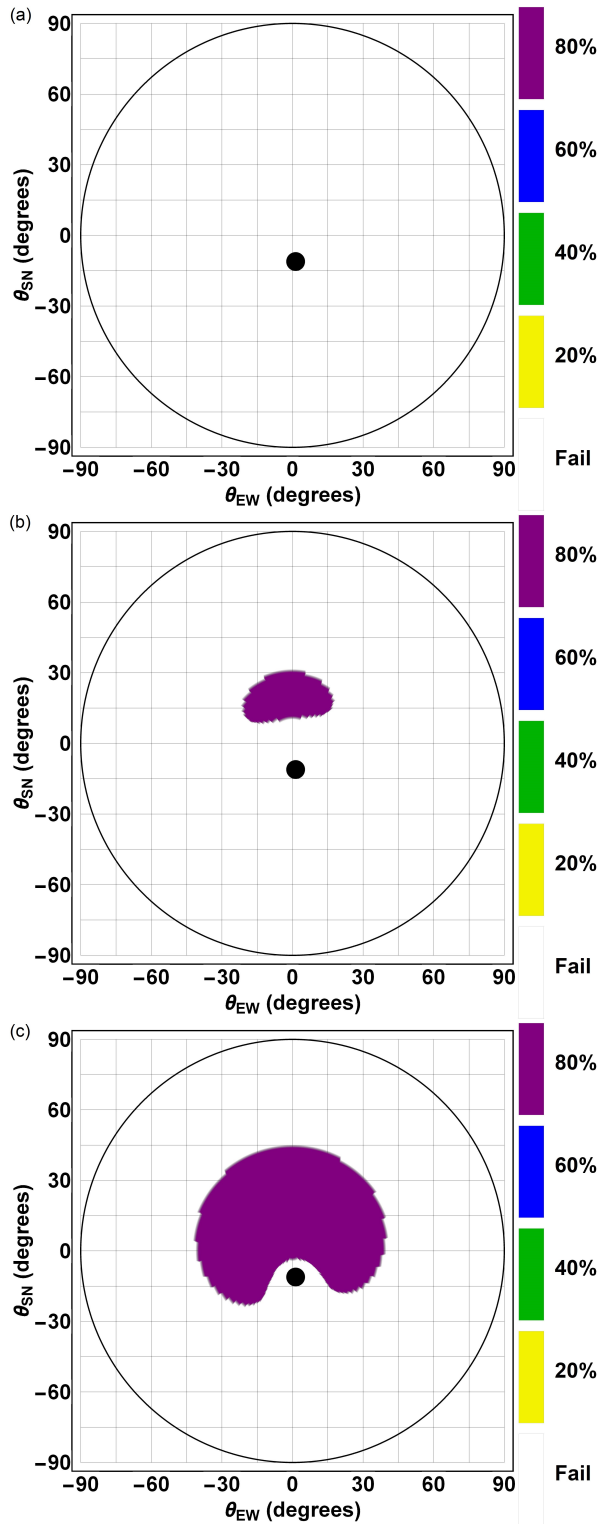


FIG. 7: Hemispherical plots of summer solstice with a $1 \times HV_{5/7}$ turbulence profile showing the regions where QTT succeeds with 99% probability for a receiver system with no higher order AO (see Sec. IV A for more details). The legend gives the heralding efficiency of the bi-photon source. In (a)–(c) we enlarge the FOV from $1 \times$ to $3 \times$ the diffraction limited FOV.

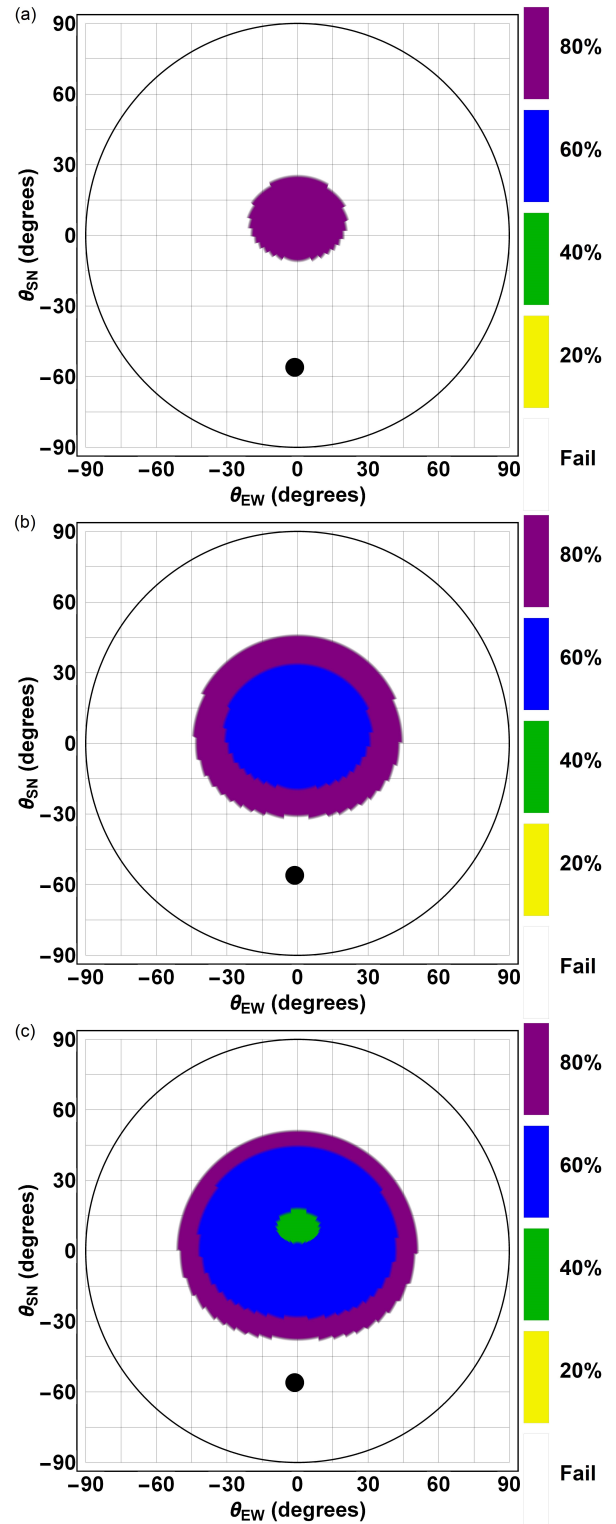


FIG. 8: Hemispherical plots of winter solstice with a $1 \times HV_{5/7}$ turbulence profile showing the regions where QTT succeeds with 99% probability for a receiver system with no higher order AO (see Sec. IV A for more details). The legend gives the heralding efficiency of the bi-photon source. In (a)–(c) we enlarge the FOV from $1 \times$ to $3 \times$ the diffraction limited FOV.

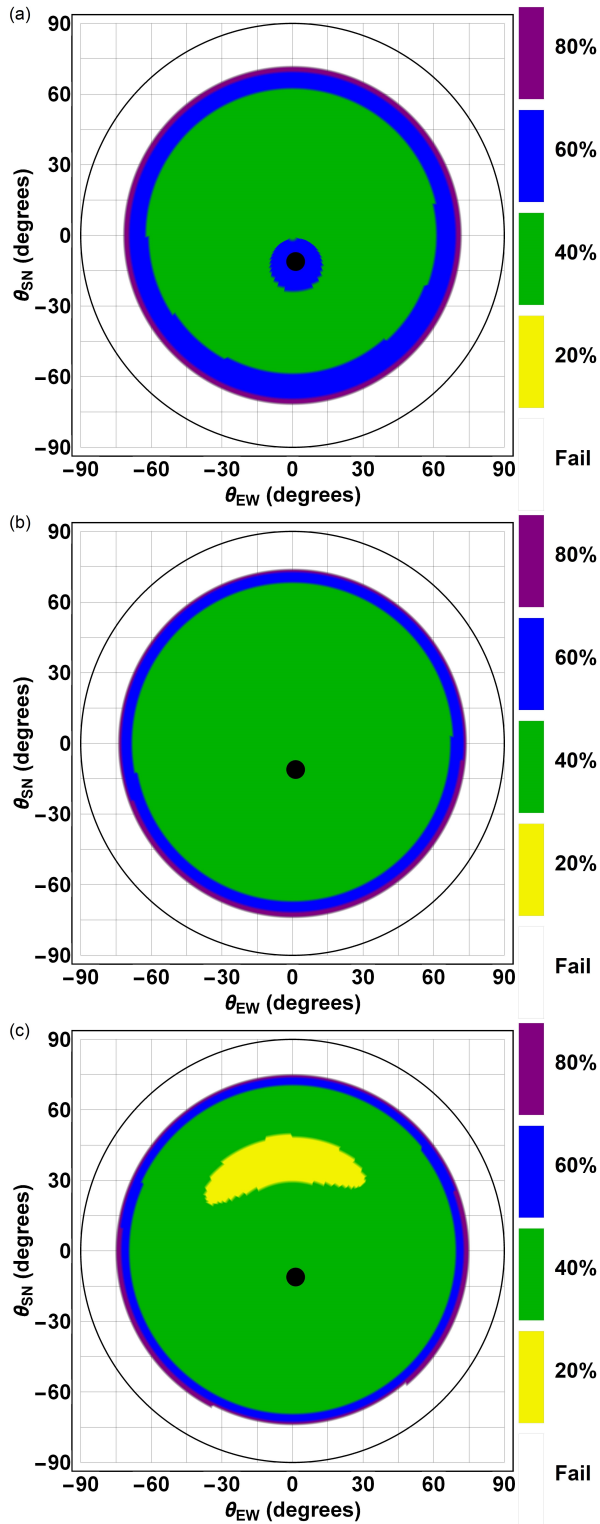


FIG. 9: Hemispherical plots of summer solstice with a $3\times HV_{5/7}$ turbulence profile showing the regions where QTT succeeds with 99% probability for a receiver system with higher order AO (see Sec. IV B for more details). The legend gives the heralding efficiency of the bi-photon source. In (a)–(c) we enlarge the FOV from $1\times$ to $3\times$ the diffraction limited FOV.

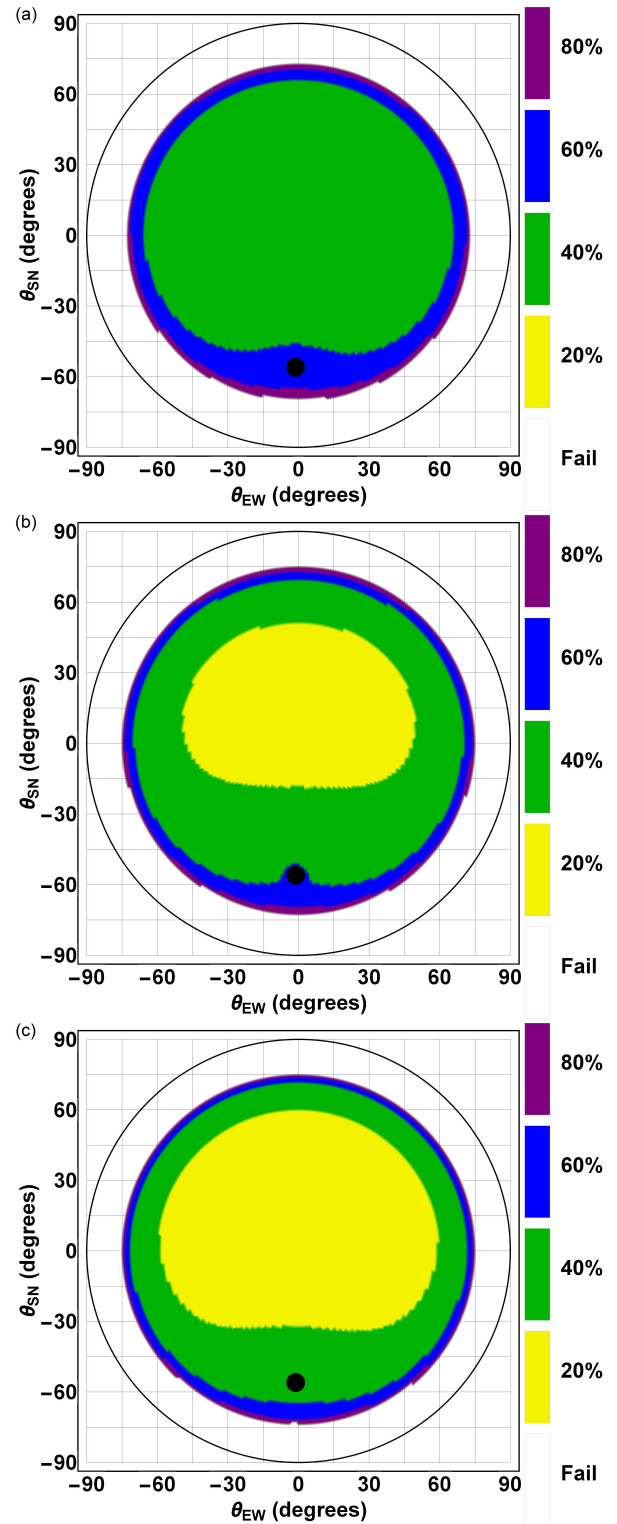


FIG. 10: Hemispherical plots of winter solstice with a $3\times HV_{5/7}$ turbulence profile showing the regions where QTT succeeds with 99% probability for a receiver system with higher order AO (see Sec. IV B for more details). The legend gives the heralding efficiency of the bi-photon source. In (a)–(c) we enlarge the FOV from $1\times$ to $3\times$ the diffraction limited FOV.

plane. In summary, the Greenwood frequency f_G characterizes the rate at which the turbulence is changing, and the Fried coherence length r_0 characterizes the spatial scale of the turbulence. The tip, tilt, and higher order correction of an AO system counteract the negative effects of these phenomenon. An AO system can be characterized by the closed-loop bandwidths of the system, and the number of wavefront sensor subapertures, and the number of actuators making up the deformable mirror (DM) that applies the correction. In the following subsections we are careful to present the residual errors that quantify the effect of these competing phenomenon.

We consider two conservative cases of optical receiver configuration. First, we assume the receiver utilizes tracking alone, that is, only tip and tilt correction, with a tracking closed-loop bandwidth $f_{TC} = 50$ Hz. Secondly, we assume the receiver is configured with both tracking and higher order AO correction utilizing $N_{act} = 25$ mirror actuators and closed loop bandwidth $f_c = 100$ Hz. In both cases, we use the aforementioned framework to map the results of our simulation to a daytime sky hemisphere to show the performance of the QTT algorithm for different heralding efficiency sources.

A. Tracking Only

In the case of utilizing tracking alone, one can estimate the residual error as a combination of the error from the higher-order structure of the signal light [23] and the finite bandwidth of the tracking system [24]

$$\sigma_{\phi,CL}^2 = 0.582 \left(\frac{D_R}{r_0} \right)^{5/3} + \left(\frac{\pi f_{TG}}{2 f_{TC}} \right)^2, \quad (8)$$

respectively, where D_R is the diameter of the receiver aperture and f_{TG} is the tracking Greenwood frequency. This residual error is inserted in place of the terms in the brackets of Eq. A9 of Ref. [22], and the rest of the framework is unaltered, except for the zenith angle dependence of the atmospheric parameters [24].

Using this map, we are able to generate hemispherical plots for two sun positions and varying turbulence strengths. The plots show the regions where QTT succeeds with 99% probability, color coded by the heralding efficiency of the biphoton source. Given the aperture sizes and channel conditions assumed, without higher-order AO, the signal attenuation will be significantly high with strong turbulence. Therefore, we assume a $1 \times HV_{5/7}$ Hufnagel-Valley turbulence profile [25], and investigate how changing the FOV of the receiver changes performance. Intuitively, since the algorithm seems highly resilient to noise, a potential strategy is to open the FOV in order to reduce channel attenuation beyond the 99% threshold. The results are given in the downward progression in Figs. 7 and 8 where the FOV increases from $1 \times$ to $3 \times$ the diffraction limited FOV. As one can see, increasing the FOV, which corresponds to a

larger field stop in the focal plane, increases the sky hemisphere accessible by QTT, despite the increased probability of noise photons. A study exploring the extent to which this strategy is successful should be included in any conceptual design. Some noteworthy concerns are the effects of the dead time of the detectors as the rates get extremely high and the potential nonuniformity of the intensity profile of the turbulence broadened signal at the spatial filter.

B. Tracking and Higher Order AO

In the case of tracking and higher order AO, one can estimate the residual error as a combination of the fitting error, aliasing error, and error due to the finite bandwidths of the tracking and higher order AO systems [24],

$$\sigma_{\phi,CL}^2 = 1.3 \times 0.28 \left(\frac{d_{sub}}{r_0} \right)^{5/3} + \left(\frac{\pi f_{TG}}{2 f_{TC}} \right)^2 + \left(\frac{f_G}{f_c} \right)^{5/3}, \quad (9)$$

where d_{sub} is the subaperture spacing, that is matched to the DM actuator spacing, and the aliasing error is set to 30% of the fitting error.

With AO, a stronger and more realistic daytime turbulence strength can be considered. In this case, we triple the turbulence strength by including a multiplicative factor on the turbulence profile, that is, we use a $3 \times HV_{5/7}$ Hufnagel-Valley profile [25]. We perform the same investigation as the previous case and open the FOV in two steps. Figures 9 and 10 give the results showing the considerable boost in performance that AO supports even in the case of $3 \times$ stronger turbulence. It also shows that good performance can be achieved using sources available today, which can have heralding efficiencies in the range of 20 to 40%, as long as AO is utilized.

In both cases, we have used conservative system parameters and restrictive constraints, e.g., 99% success probability, in order to demonstrate the utility of our methods. There is still quite a large trade space to be explored, and slight changes, for example larger aperture sizes, can make considerable changes to the results. Nonetheless, this framework can be used to model many different link conditions and the simulation results can be extended to different link budgets.

V. CONCLUSION

We investigate QTT as a candidate technique for the precise clock synchronization required to enable long-range daytime quantum networking and secure timing in GPS denied environments. The architecture is simple and the algorithm is robust to signal loss and the presence of noise photons. We characterize the performance of QTT as a function of Bob's channel attenuation and the number of noise photons present in his channel. Our results can subsequently be used to determine performance

for specific design references given a link budget has been carefully derived. Overall, our results show that QTT is resilient to attenuation and noise photons, and can reach picosecond scale precision with low heralding efficiency 2-MHz sources.

We present the probability of successful time transfer and the standard error of the mean of the clock offset, which we show is the single-shot timing precision of the QTT algorithm. We further show the standard error of the mean follows a $1/\sqrt{N_T}$ trend, where N_T is the estimate of the number of “true” coincidences between Alice and Bob. Setting a threshold probability of success to 99%, our results show how many noise photons can be withstood and how many true coincidences to expect given a certain channel loss. We also measure the Allan deviation, which conveys the stability and noise profile of the two clock system [19]. Finally, we interpret the results in the context of sky-noise photons and slant-path turbulence corresponding to a daytime space-to-Earth downlink, thereby demonstrating a specific design reference for utilizing QTT in global-scale quantum networking and timing in GPS denied environments.

ACKNOWLEDGMENTS

This work was supported by the Office of the Secretary of Defense (OSD) ARAP Defense Optical Channel Program (DOC-P). The authors acknowledge helpful discussions with Scott Newey, Boeing Corporation, and program management support from Capt. Jonathan Schiller and Valerie Knight, AFRL.

The views expressed are those of the author and do not necessarily reflect the official policy or position of the Department of the Air Force, the Department of Defense, or the U.S. government.

The appearance of external hyperlinks does not constitute endorsement by the U.S. Department of Defense (DoD) of the linked websites, or the information, products, or services contained therein. The DoD does not exercise any editorial, security, or other control over the information you may find at these locations.

-
- [1] S. Wehner, D. Elkouss, and R. Hanson, *Science* **362**, eaam9288 (2018).
 - [2] R. Van Meter, *Quantum networking* (John Wiley & Sons, 2014).
 - [3] M. Aspelmeyer, T. Jennewein, M. Pfennigbauer, W. R. Leeb, and A. Zeilinger, *IEEE Journal of Selected Topics in Quantum Electronics* **9**, 1541 (2003).
 - [4] K. Boone, J.-P. Bourgoin, E. Meyer-Scott, K. Heshami, T. Jennewein, and C. Simon, *Physical Review A* **91**, 052325 (2015).
 - [5] M. A. Lombardi, L. M. Nelson, A. N. Novick, and V. S. Zhang, *Cal Lab: International Journal of Metrology* **8**, 26 (2001).
 - [6] P. Exertier, E. Samain, N. Martin, C. Courde, M. Laas-Bourez, C. Foussard, and P. Guillemot, *Advances in Space Research* **54**, 2371 (2014).
 - [7] F. R. Giorgetta, W. C. Swann, L. C. Sinclair, E. Baumann, I. Coddington, and N. R. Newbury, *Nature Photonics* **7**, 434 (2013).
 - [8] L. C. Sinclair, W. C. Swann, H. Bergeron, E. Baumann, M. Cermak, I. Coddington, J.-D. Deschênes, F. R. Giorgetta, J. C. Juarez, I. Khader, et al., *Applied physics letters* **109**, 151104 (2016).
 - [9] L. C. Sinclair, H. Bergeron, W. C. Swann, I. Khader, K. C. Cossel, M. Cermak, N. R. Newbury, and J.-D. Deschênes, *Physical Review A* **99**, 023844 (2019).
 - [10] W. C. Swann, M. I. Bodine, I. Khader, J.-D. Deschênes, E. Baumann, L. C. Sinclair, and N. R. Newbury, *Physical Review A* **99**, 023855 (2019).
 - [11] H. Dai, Q. Shen, C.-Z. Wang, S.-L. Li, W.-Y. Liu, W.-Q. Cai, S.-K. Liao, J.-G. Ren, J. Yin, Y.-A. Chen, et al., *Nature Physics* **16**, 848 (2020).
 - [12] R. Quan, Y. Zhai, M. Wang, F. Hou, S. Wang, X. Xiang, T. Liu, S. Zhang, and R. Dong, *Scientific reports* **6**, 1 (2016).
 - [13] C. Ho, A. Lamas-Linares, and C. Kurtsiefer, *New Journal of Physics* **11**, 045011 (2009).
 - [14] J. Lee, L. Shen, A. Cerè, J. Troupe, A. Lamas-Linares, and C. Kurtsiefer, *Applied Physics Letters* **114**, 101102 (2019).
 - [15] I. Ali-Khan, C. J. Broadbent, and J. C. Howell, *Physical review letters* **98**, 060503 (2007).
 - [16] J. Mower, Z. Zhang, P. Desjardins, C. Lee, J. H. Shapiro, and D. Englund, *Physical Review A* **87**, 062322 (2013).
 - [17] C. Lee, D. Bunandar, Z. Zhang, G. R. Steinbrecher, P. B. Dixon, F. N. Wong, J. H. Shapiro, S. A. Hamilton, and D. Englund, *Optics express* **27**, 17539 (2019).
 - [18] M. Er-long, H. Zheng-fu, G. Shun-sheng, Z. Tao, D. Da-Sheng, and G. Guang-Can, *New Journal of Physics* **7**, 215 (2005).
 - [19] W. J. Riley (2008).
 - [20] D. Land, A. Levick, and J. Hand, *Measurement Science and Technology* **18**, 1917 (2007).
 - [21] N. Ashby, *Living Reviews in relativity* **6**, 1 (2003).
 - [22] R. N. Lanning, M. A. Harris, D. W. Oesch, M. D. Olike, and M. T. Gruneisen, *Phys. Rev. Applied* **16**, 044027 (2021), URL <https://link.aps.org/doi/10.1103/PhysRevApplied.16.044027>.
 - [23] R. J. Noll, *JOsA* **66**, 207 (1976).
 - [24] J. W. Hardy, *Adaptive optics for astronomical telescopes*, vol. 16 (Oxford University Press on Demand, 1998).
 - [25] R. J. Sasiela, *Electromagnetic wave propagation in turbulence: evaluation and application of Mellin transforms*, vol. 18 (Springer Science & Business Media, 2012).